

Magnitude and Spatial Distribution Control of the Supercurrent in Bi₂O₂Se-Based Josephson Junction

Jianghua Ying, Jiangbo He, Guang Yang, Mingli Liu, Zhaozheng Lyu, Xiang Zhang, Huaiyuan Liu, Kui Zhao, Ruiyang Jiang, Zhongqing Ji, Jie Fan, Changli Yang, Xiunian Jing, Guangtong Liu, Xuwei Cao, Xuefeng Wang, Li Lu,* and Fanming Qu*

Cite This: *Nano Lett.* 2020, 20, 2569–2575

Read Online

ACCESS |

Metrics & More

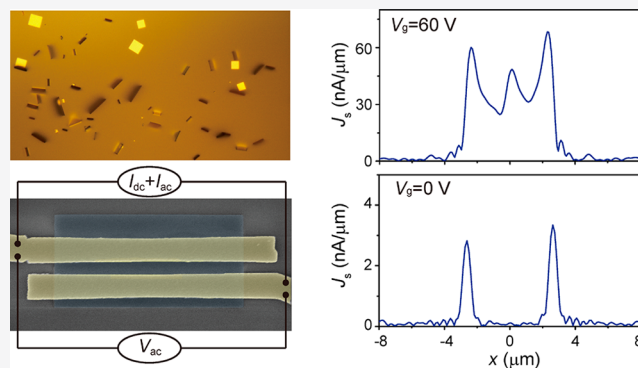
Article Recommendations

Supporting Information

ABSTRACT: Many proposals for exploring topological quantum computation are based on superconducting quantum devices constructed on materials with strong spin–orbit coupling (SOC). For these devices, full control of both the magnitude and the spatial distribution of the supercurrent is highly demanded, but has been elusive up to now. We constructed a proximity-type Josephson junction on nanoplates of Bi₂O₂Se, a new emerging semiconductor with strong SOC. Through electrical gating, we show that the supercurrent can be fully turned ON and OFF, and its real-space pathways can be configured either through the bulk or along the edges. Our work demonstrates Bi₂O₂Se as a promising platform for constructing multifunctional hybrid superconducting devices as well as for searching for topological superconductivity.

KEYWORDS: Bi₂O₂Se nanoplate, supercurrent, spatial distribution, Josephson junction

Superconducting proximity effect (SPE) allows a normal metal to superconduct when placed adjacent to a superconductor. It plays a central role in the extensive applications of superconducting quantum devices. Recently, the search for topological superconductivity has utilized SPE as a primary mechanism to construct hybrid heterostructures, since intrinsic topological superconductors (TSCs) are scarce in nature.^{1–8} Apart from being a novel topological phase of matter, TSCs afford platforms to hold Majorana zero modes (MZMs) which could be used for building fault-tolerant quantum computers.^{9–11} On this fascinating blueprint, SPE has been realized in various topological materials and semiconductors with strong spin–orbit coupling (SOC), and TSCs and MZMs have been unveiled among these hybrid structures.^{2–4,12–16} In spite of this rapid progress, for the development of electrically tunable superconducting quantum information devices, control of both the magnitude and the spatial distribution of the supercurrent in nanoscale superconducting devices is a crucial ingredient. In superconductor–normal metal–superconductor (SNS) Josephson junctions, the control of the ON/OFF of the supercurrent through electrical gating (namely supercurrent transistor) has been demonstrated in quantum dots, nanowires/nanotubes, and others.^{17–19} However, the flow path of Cooper pairs is predefined by the geometry of the devices. Regarding regulating the spatial distribution of the supercurrent, in bulk-insulating SNS junctions, Cooper pairs flow naturally on the nontrivial two-



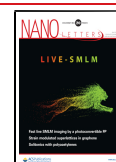
dimensional (2D) surfaces of three-dimensional (3D) topological insulators and semimetals or on the helical edges of 2D topological insulators.^{20–24} However, the supercurrent is difficult to turn OFF by gating due to the gapless nature in these topological materials. Efforts have also been put toward monitoring of the supercurrent distribution in ferromagnets and semiconductors such as InAs and graphene.^{25–31} Nevertheless, simultaneous regulation of both the magnitude and the real-space pathways of the supercurrent in SNS junctions has been elusive, especially in semiconductors with strong SOC. From a fundamental viewpoint, SOC is essential to lift the spin degeneracy and is a prerequisite for most of the materials (trivial or nontrivial) explored so far to establish TSCs.^{1–4,6,13–15,20} In this work, we address this issue and demonstrate the full control of the supercurrent through electrical gating in the Josephson junction device on a new emerging star material with strong SOC–Bi₂O₂Se nanoplates.

2D materials such as graphene, phosphorene, transition metal dichalcogenides, and topological insulators have

Received: January 3, 2020

Revised: March 22, 2020

Published: March 23, 2020



attracted tremendous interest due to their promising applications in electronics, optoelectronics, and others.^{20,21,32–34} Recently, research on a new layered semiconductor Bi₂O₂Se has been booming thanks to its superior electronic properties such as ambient stability, ultrahigh electron mobility ($\sim 2.8 \times 10^5$ cm²/V·s at 2 K), and a tunable bandgap.^{35–41} The existence of strong SOC, suppression of backscattering, as well as high-performance field-effect transistors and optoelectronics, has been experimentally demonstrated in Bi₂O₂Se thin films.^{42–46} Coherent surface states have also been examined in Bi₂O₂Se nanowires,⁴⁷ and a large Rashba SOC was further predicted to be present on the polar or nonpolar surfaces due to the intrinsic band bending.⁴⁰ These surface states reside partially in the bulk band gap, leaving appropriate space for multifunctional electrical tuning. Given these intriguing properties, Bi₂O₂Se provides opportunities to manipulate SPE and is a promising platform to engineer TSCs.

In this work, we study a Josephson junction constructed on a Bi₂O₂Se nanoplate and demonstrate the full control of the magnitude and the spatial distribution of the supercurrent through electrical gating. By employing superconducting interferometry techniques, we found that the supercurrent can be fully turned ON and OFF, and meanwhile, the supercurrent flow can be configured either through the bulk or only along the edges. Two alternative mechanisms of the bulk to edge supercurrent transition are presented.

Bi₂O₂Se nanoplates were synthesized by means of chemical vapor deposition in a horizontal tube furnace.^{35,48} Figure 1a shows an optical microscope image of the as-grown nanoplates, viewed perpendicular to the mica substrate. The nanoplates take a rectangular shape, and either lie down on the substrate or grow vertically as indicated by the red arrows in Figure 1a. The standing Bi₂O₂Se nanoplates can be easily transferred onto SiO₂/Si substrates in a purely mechanical way instead of a wet transfer process mediated by poly(methyl methacrylate), to avoid possible contamination.^{42,46} Electrode patterns were fabricated by electron-beam lithography, and Ti/Al (5 nm/65 nm) contacts were deposited by electron-beam evaporation. Note that a soft plasma cleaning of the surface of Bi₂O₂Se was performed prior to the metal deposition to improve the interface transparency. Figure 1b presents the false-colored scanning electron microscope (SEM) image of the Josephson junction device studied in this work. The Ti/Al electrodes (yellow) have a width of 560 nm each and a separation of 300 nm. The width of the Bi₂O₂Se nanoplate (dark blue) is $W = 4.6 \mu\text{m}$, and a thickness of 15 nm is confirmed by atomic force microscopy (see Supporting Information). Quasi-four terminal measurement, as depicted in Figure 1b, was performed with standard low-frequency lock-in techniques in a dilution refrigerator at a base temperature of ~ 10 mK. A gate voltage V_g was applied through the degenerately doped Si substrate covered with 300-nm-thick SiO₂.

For SNS Josephson junctions, superconducting interferometry is a convenient and powerful technique to discriminate the spatial distribution of the supercurrent.^{20,21,27} The supercurrent–density profile can be extracted from the perpendicular magnetic field dependence of the critical current, I_c vs B_z , through the Dynes–Fulton approach.⁴⁹ Figure 1c illustrates the correspondence between the interference patterns (right column) and the supercurrent density as a function of position, $J_s(x)$ (left column). For a spatially uniform supercurrent (top row), which is usually the case for a bulk conducting junction,

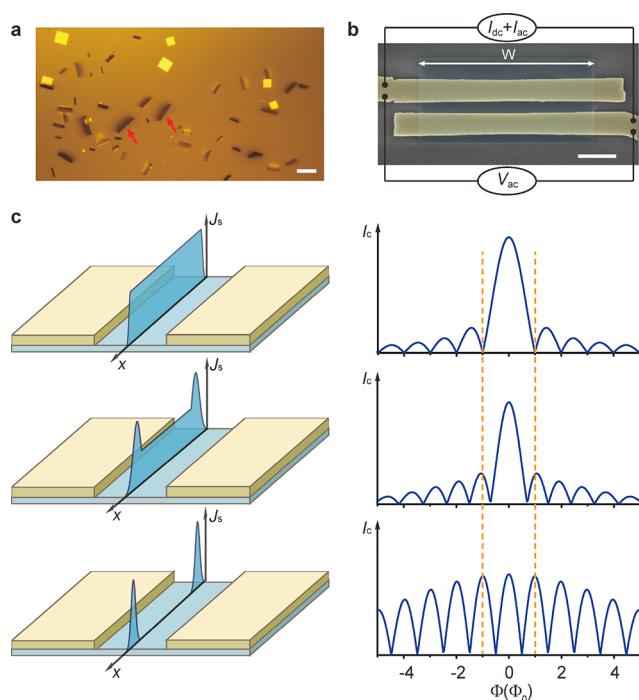


Figure 1. Device and superconducting interferometry. a. Optical microscope image of the as-grown Bi₂O₂Se nanoplates, with a rectangular shape, either lying or standing (as indicated by the red arrows) on the mica substrate. Scale bar: 10 μm . b. False-colored scanning electron microscope image of the Josephson junction studied. Scale bar: 1 μm . Two Ti/Al electrodes (yellow) contact the Bi₂O₂Se nanoplate (dark blue) forming a proximity-type Josephson junction. The circuit displays the quasi-four terminal measurement configurations. c. Correspondence between the supercurrent–density profile, $J_s(x)$, in a Josephson junction (left column) and the superconducting interference pattern, i.e., the dependence of critical current I_c on magnetic flux Φ in the junction area (right column). The two dashed lines indicate the shift of the positions of the first nodes relative to the one-slit Fraunhofer-like pattern (top right).

$I_c(B_z)$ presents a one-slit Fraunhofer-like pattern following the form $|\sin(\pi\Phi/\Phi_0)/(\pi\Phi/\Phi_0)|$, where $\Phi = L_{\text{eff}}WB_z$ is the flux, L_{eff} and W are the effective length and width of the junction, respectively, and $\Phi_0 = h/2e$ is the flux quantum (h is the Planck constant, e the elementary charge). The central lobe of $I_c(B_z)$ has a width of $2\Phi_0$ and the side lobes of Φ_0 . In addition, the height of the lobes shows an overall $1/|B_z|$ decay. When the supercurrent flows along the two edges (bottom row), the single junction mimics a superconducting quantum interference device (SQUID) and presents a two-slit interference pattern with the form $|\cos(\pi\Phi/\Phi_0)|$. The lobes in this case have a uniform width of Φ_0 and a weak overall decay (the decrease mainly results from the suppression of the superconductivity in the contacts and a finite width of the edge modes).⁵⁰ In the intermediate regime (middle row), bulk and edge supercurrent coexist, and $I_c(B_z)$ exhibits a one-slit to two-slit transition. Generally speaking, $I_c(B_z)$ and $J_s(x)$ can be extracted quantitatively from each other through integration or Fourier transform.⁴⁹

We first present the gate tuning of the magnitude of the supercurrent between the ON and OFF states. Figure 2a,b shows the differential resistance $dV/dI \equiv V_{\text{ac}}/I_{\text{ac}}$ as a function of gate voltage V_g and dc bias current I_{dc} . To reach a high contrast and a clear view of the color map, we divided the full V_g range of -10 to 60 V into these two subranges and plotted

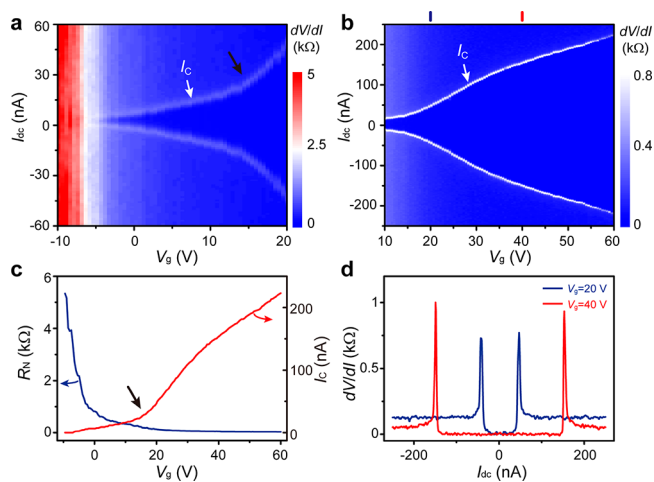


Figure 2. Gate-tunable ON and OFF states of the supercurrent. a, b. Differential resistance dV/dI as a function of both gate voltage V_g and dc bias current I_{dc} in two gate-voltage ranges for clarity. The white arrows mark the critical current I_c . c. V_g dependent normal state resistance R_N and I_c extracted from a and b. d. Typical line cuts at $V_g = 40$ V (red) and 20 V (blue) taken from b as marked by the red and blue bars, showing the superconducting and normal states at low and high bias current, respectively. The black arrows in a and c guide the upturn of I_c around $V_g = 15$ V.

them in two different color scales. The dV/dI peaks, as indicated by the white arrows, correspond to the critical current I_c , separating the zero-resistance state (uniform blue color) at low $|I_{dc}|$ from the normal state at high $|I_{dc}|$. Two typical line cuts are plotted in Figure 2d, taken at $V_g = 20$ V (blue) and 40 V (red), respectively. Figure 2c shows the gate voltage dependence of the normal-state resistance R_N and I_c extracted from Figure 2a and b. When sweeping V_g from 60 V to -10 V, R_N increases monotonically toward infinite (~ 50 k Ω at $V_g = -20$ V, data not shown), which is expected as the electrons are depleted. Meanwhile, I_c decreases also monotonically from 223 nA at $V_g = 60$ V to 0 nA around $V_g = -7$ V. Therefore, the supercurrent can be fully turned ON/OFF by gating. Note that the black arrows in Figure 2a,c indicate the upturn of I_c around $V_g = 15$ V, which will be discussed later. The $I_c R_N$ product is about 8 μ V at $V_g = 60$ V, with an energy scale much smaller than the superconducting gap of Al, indicating a low-transparency interface.

Next, we switch to the superconducting interference and disentangle the bulk and edge supercurrent. To do so, a perpendicular magnetic field B_z was applied to the junction. Figure 3a shows the differential resistance dV/dI as a function of both B_z and I_{dc} at $V_g = 60, 40, 20,$ and 0 V, respectively. The whitish envelope characterizes the critical current I_c and separates the superconducting and normal states. At $V_g = 60$ V, I_c presents a one-slit Fraunhofer-like pattern, with a central lobe of width roughly twice the side lobes and also a global fast decay. The average period of $\Delta B_z \approx 5.1$ G agrees with the dimension of the junction $-\Phi_0/L_{eff}W = 5.2$ G, where $L_{eff} = 860$ nm is the effective length of the junction considering the flux focusing effect of the contacts. The two dashed lines illustrate the positions of the first nodes. At $V_g = 40$ V, not much changes but a smaller I_c as the carrier density reduces. When V_g decreases further to 20 V, the first lobe shrinks in both width and amplitude, and the nodes move toward zero B_z . Moreover, the overall decay of I_c slows down, indicating a transition from bulk to edge supercurrent. Finally, at $V_g = 0$ V,

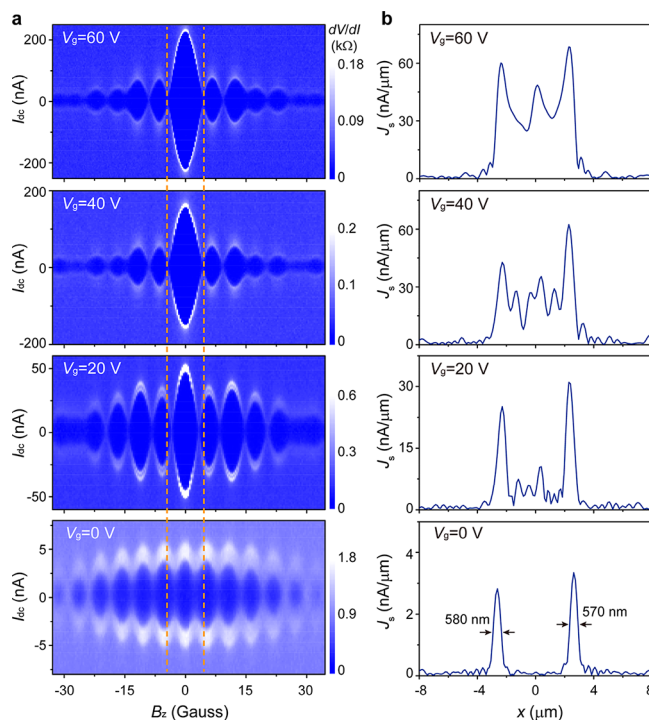


Figure 3. Bulk to edge supercurrent transition. a. Superconducting interference patterns—differential resistance dV/dI as a function of perpendicular magnetic field B_z and dc bias current I_{dc} , at $V_g = 60, 40, 20,$ and 0 V, respectively. The two dashed lines illustrate the shift of the first nodes. b. supercurrent-density $J_g(x)$ retrieved from a at different gate voltages accordingly, through the Dynes–Fulton approach. $x = 0$ corresponds to the center of the junction. The fwhm of the left and right peak when $V_g = 0$ V are 580 and 570 nm, respectively.

a clear two-slit SQUID pattern appears, while the nodes move further inward, forming equally spaced, weakly decayed lobes, which signals edge-mode superconductivity.

The analysis above can also be investigated by using the Dynes–Fulton approach to extract the supercurrent-density profile. Figure 3b displays the position (x) dependence of J_g at different V_g , obtained from the Fourier transform of the I_c vs B_z curves retrieved from Figure 3a accordingly. Note that $x = 0$ corresponds to the center of the junction. The bulk-dominated supercurrent at $V_g = 60$ and 40 V, the bulk to edge transition at $V_g = 20$ V, and the edge-dominated supercurrent at $V_g = 0$ V can be immediately recognized. Therefore, through electrical gating, we realized the configuration of the supercurrent pathways.

We now discuss the underlying mechanism of the gate tuning of the supercurrent distribution. Although the Fraunhofer to SQUID evolution and the supercurrent-density profiles demonstrate the “bulk” to edge supercurrent transition, it is ambiguous that if the “bulk” is the 3D bulk or, alternatively, the top and bottom surfaces. These two scenarios arise from the Se or Bi termination-sensitive surface states in $\text{Bi}_2\text{O}_2\text{Se}$.

For Se-terminated (001) surface, Figure 4a sketches the band structure (not to scale) around the Γ point, including the spin-split subbands (blue) close to the valence band. Regarding the fact that when sweeping V_g from 60 V to -10 V, the normal state resistance increases monotonically toward infinite, the conduction band of the (3D) bulk undertakes the electron transport, as indicated by the blue shaded region. However, the

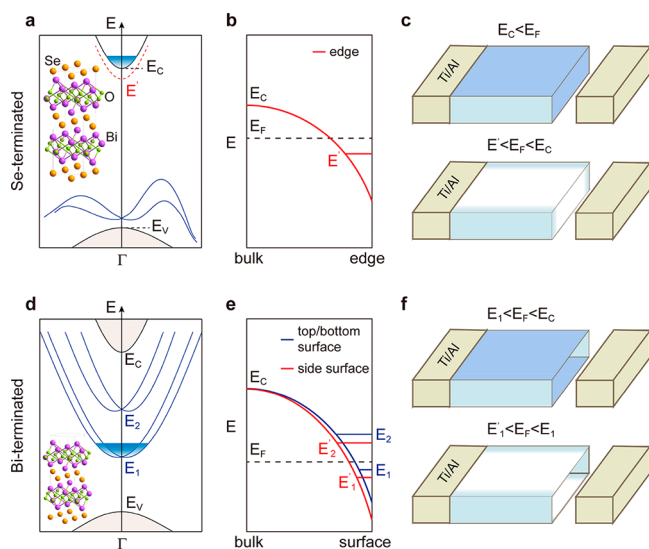


Figure 4. Mechanisms of the bulk to edge supercurrent transition. a,d. Sketches of the band structure of the Se-terminated (a) and Bi-terminated (d) (001) surface around the Γ point.⁴⁰ The spin-split surface states are represented by the blue lines. The blue shaded regions indicate the range corresponding to the gate-voltage applied in this study. The insets present the Se- and Bi-terminated (001) surface, respectively. b. Effective band bending at the edges of the $\text{Bi}_2\text{O}_2\text{Se}$ nanoplate for Se-terminated top/bottom surfaces and the formation of the edge states. c. Illustration of the bulk-dominated (top panel) and the edge-dominated (bottom panel) supercurrent for Se-terminated case, with the blue color indicating the supercurrent pathways. For clarity, the right Ti/Al contacts are moved apart. e. Effective band bending at the surfaces for the Bi-terminated case and the formation of the surface subbands which are assumed to be slightly lower for the side surface (red) than that for the top/bottom surface (blue). f. Illustration of the top and bottom surfaces dominated (top panel) and the side surfaces dominated (bottom panel) supercurrent for the Bi-terminated case.

bulk to edge supercurrent transition suggests the existence of edge states, presumably due to downward band bending at the edges.^{26,40,51} Figure 4b displays such band bending and the formation of the edge states (at energy E'), as illustrated by the red dashed line in Figure 4a. Consequently, edge supercurrent dominates when the Fermi level E_F sits between E' and the bottom of the conduction band E_C (bottom panel of Figure 4c). The upturn of the critical current around $V_g = 15$ V, as guided by the black arrows in Figure 2a and c, corresponds to the onset of the 3D bulk supercurrent when $E_F > E_C$ (top panel of Figure 4c), consistent with the observation of finite J_s in the bulk at $V_g = 20$ V (Figure 3).

The scenario for Bi-terminated top/bottom surface is completely different.⁴⁰ Figure 4d sketches the band structure (not to scale) around Γ point, including the two spin-split subbands (blue) on (001) surface. According to ref 40, the separation between the subband bottoms is $E_2 - E_1 \approx 0.34$ eV. We assign $V_g = -10$ V to correspond to a Fermi level position just below E_1 , since the junction tends to be insulating. Thus, the Fermi level position

$$E_F(V_g) = \pi \hbar^2 n / 2m^* + E_1, \quad \text{where } n \text{ is the 2D} \\ = \pi \hbar^2 \epsilon (V_g + 10\text{V}) / 2edm^* + E_1$$

electron density induced by the gate, a factor of 2 denotes an equal footing of the top and bottom surfaces, ϵ is the dielectric constant of SiO_2 , $d = 300$ nm is the thickness of SiO_2 , and m^*

$= 0.14m_0$ the effective electron mass of $\text{Bi}_2\text{O}_2\text{Se}$ (m_0 is the electron mass).³⁵ At $V_g = 60$ V, E_F sits ~ 0.04 eV above E_1 , far below E_2 and the conduction band E_C . Hence, in the gate-voltage range studied, as indicated by the blue shaded region in Figure 4d, electrons are only induced on the surfaces of the $\text{Bi}_2\text{O}_2\text{Se}$ nanoplate, but not in the 3D bulk. Consequently, the “bulk” supercurrent mentioned above flows actually through the top and bottom surfaces. We would like to note that there can be a difference between these two surfaces due to the gate being at the bottom and the contacts being on the top.

Similarly, the bulk to edge transition indicates a slightly different E_1 (onset energy) between the top/bottom surfaces and the side surfaces. Under this assumption, Figure 4e illustrates such effective band bending and the formation of the surface subbands. When E_F sits above E_1 , the top and bottom surfaces dominate the supercurrent with relatively small contributions from the side surfaces considering the small thickness of 15 nm (top panel of Figure 4f). However, within the narrow energy window between E'_1 and E_1 , the side surfaces dominate (bottom panel of Figure 4f). Again, the upturn of I_c around $V_g = 15$ V implies the onset of the supercurrent on the top and bottom surfaces.

For both Se and Bi terminations, however, the full width at half-maximum (fwhm) of the edge-supercurrent density peak, ~ 570 nm (see bottom right panel in Figure 3b), is much larger than the typical thickness of surface states, say, several nanometers.^{40,52} This can be explained by the extension of the 2D electron waves from the edge to the 3D bulk for the Se-terminated case (from side surfaces to the top and bottom surfaces for Bi-terminated case) with an order of the Fermi wavelength, as observed in graphene.²⁷ Such an explanation is further corroborated by the decay of the supercurrent density from the edge toward the center of the junction (see Supporting Information). Notably, these two scenarios are very interesting, although the current study could not differentiate between the Se- or Bi-terminated surfaces, and alternative interpretations for the edge supercurrent may also apply. Therefore, detailed studies are required to nail down more exquisite physical pictures. Note that the crystal structure, the thickness, and the edge characteristics of $\text{Bi}_2\text{O}_2\text{Se}$ nanoplates are different from gapped graphene, so that the mechanism for the transition of the supercurrent distribution belongs to different scenarios.²⁸

In summary, we fabricated a Josephson junction device on a $\text{Bi}_2\text{O}_2\text{Se}$ nanoplate and realized a superconducting proximity effect. Through electrical gating, the supercurrent can be fully turned ON and OFF, and simultaneously, the supercurrent spatial distribution can be configured in the bulk or along the edges. The termination-sensitive surface states render plentiful mechanisms and various possible configurations, and leave extensive room for multifunctional electrical tuning. Considering the remarkable properties and the strong spin-orbit coupling, $\text{Bi}_2\text{O}_2\text{Se}$ is a promising platform for studying numerous novel phenomena, such as constructing gate controllable hybrid superconducting devices,¹⁸ supercurrent field-effect transistors,¹⁹ nanoscale SQUID,⁵³ superconducting optoelectronics,⁵⁴ Josephson laser,⁵⁵ Cooper-pair beam splitter,⁵⁶ and engineering topological superconductors.^{2,3,6}

■ ASSOCIATED CONTENT

Supporting Information

The Supporting Information is available free of charge at <https://pubs.acs.org/doi/10.1021/acs.nanolett.0c00025>.

Synthesis and characterization of Bi₂O₂Se nanoplates; Device fabrication; Low-temperature transport measurement; Extraction of the supercurrent–density profile; Comparison between different devices (PDF)

■ AUTHOR INFORMATION

Corresponding Authors

Li Lu – Beijing National Laboratory for Condensed Matter Physics, Institute of Physics, Chinese Academy of Sciences, Beijing 100190, China; School of Physical Sciences and CAS Center for Excellence in Topological Quantum Computation, University of Chinese Academy of Sciences, Beijing 100049, China; Songshan Lake Materials Laboratory, Dongguan, Guangdong 523808, China; Beijing Academy of Quantum Information Sciences, Beijing 100193, China; Email: lulu@iphy.ac.cn

Fanming Qu – Beijing National Laboratory for Condensed Matter Physics, Institute of Physics, Chinese Academy of Sciences, Beijing 100190, China; School of Physical Sciences and CAS Center for Excellence in Topological Quantum Computation, University of Chinese Academy of Sciences, Beijing 100049, China; Songshan Lake Materials Laboratory, Dongguan, Guangdong 523808, China; orcid.org/0000-0001-6660-9335; Email: fanmingqu@iphy.ac.cn

Authors

Jianghua Ying – Beijing National Laboratory for Condensed Matter Physics, Institute of Physics, Chinese Academy of Sciences, Beijing 100190, China; School of Physical Sciences, University of Chinese Academy of Sciences, Beijing 100049, China

Jiangbo He – Beijing National Laboratory for Condensed Matter Physics, Institute of Physics, Chinese Academy of Sciences, Beijing 100190, China; School of Physical Sciences, University of Chinese Academy of Sciences, Beijing 100049, China

Guang Yang – Beijing National Laboratory for Condensed Matter Physics, Institute of Physics, Chinese Academy of Sciences, Beijing 100190, China; School of Physical Sciences, University of Chinese Academy of Sciences, Beijing 100049, China

Mingli Liu – Beijing National Laboratory for Condensed Matter Physics, Institute of Physics, Chinese Academy of Sciences, Beijing 100190, China; School of Physical Sciences, University of Chinese Academy of Sciences, Beijing 100049, China

Zhaozheng Lyu – Beijing National Laboratory for Condensed Matter Physics, Institute of Physics, Chinese Academy of Sciences, Beijing 100190, China; School of Physical Sciences, University of Chinese Academy of Sciences, Beijing 100049, China

Xiang Zhang – Beijing National Laboratory for Condensed Matter Physics, Institute of Physics, Chinese Academy of Sciences, Beijing 100190, China; School of Physical Sciences, University of Chinese Academy of Sciences, Beijing 100049, China

Huaiyuan Liu – Beijing National Laboratory for Condensed Matter Physics, Institute of Physics, Chinese Academy of Sciences, Beijing 100190, China; School of Physics, Nankai University, Tianjin 300071, China

Kui Zhao – Beijing National Laboratory for Condensed Matter Physics, Institute of Physics, Chinese Academy of Sciences, Beijing 100190, China; School of Physical Sciences, University of Chinese Academy of Sciences, Beijing 100049, China

Ruiyang Jiang – Beijing National Laboratory for Condensed Matter Physics, Institute of Physics, Chinese Academy of Sciences, Beijing 100190, China; School of Physical Sciences, University of Chinese Academy of Sciences, Beijing 100049, China

Zhongqing Ji – Beijing National Laboratory for Condensed Matter Physics, Institute of Physics, Chinese Academy of Sciences, Beijing 100190, China; Songshan Lake Materials Laboratory, Dongguan, Guangdong 523808, China

Jie Fan – Beijing National Laboratory for Condensed Matter Physics, Institute of Physics, Chinese Academy of Sciences, Beijing 100190, China; Songshan Lake Materials Laboratory, Dongguan, Guangdong 523808, China

Changli Yang – Beijing National Laboratory for Condensed Matter Physics, Institute of Physics, Chinese Academy of Sciences, Beijing 100190, China

Xiunian Jing – Beijing National Laboratory for Condensed Matter Physics, Institute of Physics, Chinese Academy of Sciences, Beijing 100190, China; Songshan Lake Materials Laboratory, Dongguan, Guangdong 523808, China

Guangtong Liu – Beijing National Laboratory for Condensed Matter Physics, Institute of Physics, Chinese Academy of Sciences, Beijing 100190, China; Songshan Lake Materials Laboratory, Dongguan, Guangdong 523808, China

Xuewei Cao – School of Physics, Nankai University, Tianjin 300071, China

Xuefeng Wang – National Laboratory of Solid State Microstructures, Collaborative Innovation Center of Advanced Microstructures, School of Electronic Science and Engineering, Nanjing University, Nanjing 210093, China; orcid.org/0000-0002-3472-7895

Complete contact information is available at: <https://pubs.acs.org/10.1021/acs.nanolett.0c00025>

Author Contributions

L.L. and F.Q. supervised the overall research. J.Y. and R.J. synthesized the material. J.Y. fabricated the device and carried out the measurement with the assistance from J.H., G.Y., M.L., Z.L., X.Z., H.L., K.Z., R.J., Z.J., J.F., C.Y., X.J., G.L., L.L., and F.Q. All authors participated in the analysis of the data. F.Q., J.Y., and L.L. wrote the paper under constructive discussions with all other authors.

Notes

The authors declare no competing financial interest.

■ ACKNOWLEDGMENTS

We would like to thank Hailin Peng and Ning Kang for fruitful discussions. This work was supported by the National Basic Research Program of China from the MOST grants 2017YFA0304700, 2016YFA0300601, and 2015CB921402, by the NSF China grants 11527806, 91221203, 11174357, 91421303, 11774405, and 61822403, by the Strategic Priority Research Program B of Chinese Academy of Sciences, Grants No. XDB28000000 and XDB07010100, by the Beijing Municipal Science & Technology Commission, China, Grant No. Z191100007219008, by the Open Research Fund from State Key Laboratory of High Performance Computing of China, and by Beijing Academy of Quantum Information Sciences, Grant No. Y18G08.

■ REFERENCES

- (1) Qi, X.-L.; Zhang, S.-C. Topological insulators and superconductors. *Rev. Mod. Phys.* **2011**, *83*, 1057–1110.
- (2) Ren, H.; et al. Topological superconductivity in a phase-controlled Josephson junction. *Nature* **2019**, *569*, 93–98.
- (3) Fornieri, A.; et al. Evidence of topological superconductivity in planar Josephson junctions. *Nature* **2019**, *569*, 89–92.
- (4) Mourik, V.; et al. Signatures of Majorana Fermions in Hybrid Superconductor-Semiconductor Nanowire Devices. *Science* **2012**, *336*, 1003–1007.
- (5) Fu, L.; Kane, C. L. Superconducting Proximity Effect and Majorana Fermions at the Surface of a Topological Insulator. *Phys. Rev. Lett.* **2008**, *100*, 096407.
- (6) Pientka, F.; et al. Topological Superconductivity in a Planar Josephson Junction. *Phys. Rev. X* **2017**, *7*, 021032.
- (7) Oreg, Y.; Refael, G.; von Oppen, F. Helical Liquids and Majorana Bound States in Quantum Wires. *Phys. Rev. Lett.* **2010**, *105*, 177002.
- (8) Lutchyn, R. M.; Sau, J. D.; Das Sarma, S. Majorana Fermions and a Topological Phase Transition in Semiconductor-Superconductor Heterostructures. *Phys. Rev. Lett.* **2010**, *105*, 077001.
- (9) Wilczek, F. Majorana returns. *Nat. Phys.* **2009**, *5*, 614–618.
- (10) Sarma, S. D.; Freedman, M.; Nayak, C. Majorana zero modes and topological quantum computation. *Npj Quantum Information* **2015**, *1*, 15001.
- (11) Kitaev, A. Y. Fault-tolerant quantum computation by anyons. *Ann. Phys.* **2003**, *303*, 2–30.
- (12) Deng, M. T.; et al. Majorana bound state in a coupled quantum-dot hybrid-nanowire system. *Science* **2016**, *354*, 1557–1562.
- (13) Yang, G.; et al. Protected gap closing in Josephson trijunctions constructed on Bi₂Te₃. *Phys. Rev. B: Condens. Matter Mater. Phys.* **2019**, *100*, 180501.
- (14) Bocquillon, E.; et al. Gapless Andreev bound states in the quantum spin Hall insulator HgTe. *Nat. Nanotechnol.* **2017**, *12*, 137.
- (15) Xu, J.-P.; et al. Experimental Detection of a Majorana Mode in the core of a Magnetic Vortex inside a Topological Insulator-Superconductor Bi₂Te₃/NbSe₂ Heterostructure. *Phys. Rev. Lett.* **2015**, *114*, 017001.
- (16) Nadj-Perge, S.; et al. Observation of Majorana fermions in ferromagnetic atomic chains on a superconductor. *Science* **2014**, *346*, 602–607.
- (17) Doh, Y.-J.; et al. Tunable Supercurrent Through Semiconductor Nanowires. *Science* **2005**, *309*, 272–275.
- (18) De Franceschi, S.; Kouwenhoven, L.; Schönberger, C.; Wernsdorfer, W. Hybrid superconductor-quantum dot devices. *Nat. Nanotechnol.* **2010**, *5*, 703.
- (19) Jarillo-Herrero, P.; van Dam, J. A.; Kouwenhoven, L. P. Quantum supercurrent transistors in carbon nanotubes. *Nature* **2006**, *439*, 953–956.
- (20) Hart, S.; et al. Induced superconductivity in the quantum spin Hall edge. *Nat. Phys.* **2014**, *10*, 638–643.
- (21) Pribiag, V. S.; et al. Edge-mode superconductivity in a two-dimensional topological insulator. *Nat. Nanotechnol.* **2015**, *10*, 593–597.
- (22) Huang, C.; et al. Proximity-induced surface superconductivity in Dirac semimetal Cd₃As₂. *Nat. Commun.* **2019**, *10*, 2217.
- (23) Veldhorst, M.; et al. Josephson supercurrent through a topological insulator surface state. *Nat. Mater.* **2012**, *11*, 417–421.
- (24) Schindler, F.; et al. Higher-order topology in bismuth. *Nat. Phys.* **2018**, *14*, 918–924.
- (25) Lahabi, K.; et al. Controlling supercurrents and their spatial distribution in ferromagnets. *Nat. Commun.* **2017**, *8*, 2056.
- (26) de Vries, F. K.; et al. h/e Superconducting Quantum Interference through Trivial Edge States in InAs. *Phys. Rev. Lett.* **2018**, *120*, 047702.
- (27) Allen, M. T.; et al. Spatially resolved edge currents and guided-wave electronic states in graphene. *Nat. Phys.* **2016**, *12*, 128.
- (28) Zhu, M. J.; et al. Edge currents shunt the insulating bulk in gapped graphene. *Nat. Commun.* **2017**, *8*, 14552.
- (29) Calado, V. E.; et al. Ballistic Josephson junctions in edge-contacted graphene. *Nat. Nanotechnol.* **2015**, *10*, 761–764.
- (30) Ben Shalom, M.; et al. Quantum oscillations of the critical current and high-field superconducting proximity in ballistic graphene. *Nat. Phys.* **2016**, *12*, 318–322.
- (31) Amet, F.; et al. Supercurrent in the quantum Hall regime. *Science* **2016**, *352*, 966–969.
- (32) Novoselov, K. S.; et al. Electric Field Effect in Atomically Thin Carbon Films. *Science* **2004**, *306*, 666–669.
- (33) Radisavljevic, B.; Radenovic, A.; Brivio, J.; Giacometti, V.; Kis, A. Single-layer MoS₂ transistors. *Nat. Nanotechnol.* **2011**, *6*, 147.
- (34) Li, L.; et al. Black phosphorus field-effect transistors. *Nat. Nanotechnol.* **2014**, *9*, 372.
- (35) Wu, J.; et al. High electron mobility and quantum oscillations in non-encapsulated ultrathin semiconducting Bi₂O₂Se. *Nat. Nanotechnol.* **2017**, *12*, 530.
- (36) Chen, C.; et al. Electronic structures and unusually robust bandgap in an ultrahigh-mobility layered oxide semiconductor, Bi₂O₂Se. *Science Advances* **2018**, *4*, No. eaat8355.
- (37) Fu, H.; Wu, J.; Peng, H.; Yan, B. Self-modulation doping effect in the high-mobility layered semiconductor Bi₂O₂Se. *Phys. Rev. B: Condens. Matter Mater. Phys.* **2018**, *97*, 241203.
- (38) Khan, U.; et al. Controlled Vapor-Solid Deposition of Millimeter-Size Single Crystal 2D Bi₂O₂Se for High-Performance Phototransistors. *Adv. Funct. Mater.* **2019**, *29*, 1807979.
- (39) Liang, Y.; et al. Molecular Beam Epitaxy and Electronic Structure of Atomically Thin Oxyselenide Films. *Adv. Mater.* **2019**, *31*, 1901964.
- (40) Ereemeev, S. V.; Koroteev, Y. M.; Chulkov, E. V. Surface electronic structure of bismuth oxychalcogenides. *Phys. Rev. B: Condens. Matter Mater. Phys.* **2019**, *100*, 115417.
- (41) Ghosh, T.; et al. Ultrathin Free-Standing Nanosheets of Bi₂O₂Se: Room Temperature Ferroelectricity in Self-Assembled Charged Layered Heterostructure. *Nano Lett.* **2019**, *19*, 5703–5709.
- (42) Meng, M.; et al. Strong spin-orbit interaction and magnetotransport in semiconductor Bi₂O₂Se nanoplates. *Nanoscale* **2018**, *10*, 2704–2710.
- (43) Tong, T.; et al. Ultrahigh Hall mobility and suppressed backward scattering in layered semiconductor Bi₂O₂Se. *Appl. Phys. Lett.* **2018**, *113*, 072106.
- (44) Li, J.; et al. High-Performance Near-Infrared Photodetector Based on Ultrathin Bi₂O₂Se Nanosheets. *Adv. Funct. Mater.* **2018**, *28*, 1706437.
- (45) Tian, X.; et al. An Ultrabroadband Mid-Infrared Pulsed Optical Switch Employing Solution-Processed Bismuth Oxyselenide. *Adv. Mater.* **2018**, *30*, 1801021.
- (46) Fu, Q.; et al. Ultrasensitive 2D Bi₂O₂Se Phototransistors on Silicon Substrates. *Adv. Mater.* **2019**, *31*, 1804945.
- (47) Ying, J.; et al. Gate-tunable h/e -period magnetoresistance oscillations in Bi₂O₂Se nanowires. *Phys. Rev. B: Condens. Matter Mater. Phys.* **2019**, *100*, 235307.
- (48) Wu, Z.; et al. Seed-Induced Vertical Growth of 2D Bi₂O₂Se Nanoplates by Chemical Vapor Transport. *Adv. Funct. Mater.* **2019**, *29*, 1906639.
- (49) Dynes, R. C.; Fulton, T. A. Supercurrent Density Distribution in Josephson Junctions. *Phys. Rev. B* **1971**, *3*, 3015–3023.
- (50) Qu, F.; et al. Strong Superconducting Proximity Effect in Pb-Bi₂Te₃ Hybrid Structures. *Sci. Rep.* **2012**, *2*, 339.
- (51) King, P. D. C.; et al. Large Tunable Rashba Spin Splitting of a Two-Dimensional Electron Gas in Bi₂Se₃. *Phys. Rev. Lett.* **2011**, *107*, 096802.
- (52) Zhang, Y.; et al. Crossover of the three-dimensional topological insulator Bi₂Se₃ to the two-dimensional limit. *Nat. Phys.* **2010**, *6*, 584–588.
- (53) Vasyukov, D.; et al. A scanning superconducting quantum interference device with single electron spin sensitivity. *Nat. Nanotechnol.* **2013**, *8*, 639–644.
- (54) Recher, P.; Nazarov, Y. V.; Kouwenhoven, L. P. Josephson Light-Emitting Diode. *Phys. Rev. Lett.* **2010**, *104*, 156802.

(55) Cassidy, M. C.; et al. Demonstration of an ac Josephson junction laser. *Science* **2017**, *355*, 939.

(56) Hofstetter, L.; Csonka, S.; Nygård, J.; Schönenberger, C. Cooper pair splitter realized in a two-quantum-dot Y-junction. *Nature* **2009**, *461*, 960–963.